



Sources of riverine mercury across the Mackenzie River Basin; inferences from a combined Hg—C isotopes and optical properties approach



Audrey Campeau^{a,g,*}, Karin Eklöf^b, Anne L. Soerensen^c, Staffan Åkerblom^d, Shengliu Yuan^e, Holger Hintelmann^e, Magdalena Bieroza^f, Stephan Köhler^b, Christian Zdanowicz^a

^a Department of Earth Sciences, Uppsala University, Sweden

^b Department of Aquatic Sciences and Assessment, Swedish University of Agricultural Sciences, Uppsala, Sweden

^c Department of Environmental Research and Monitoring, Swedish Museum of Natural History, Sweden

^d Statistiska centralbyrån (SCB), Statistic Sweden, Stockholm, Sweden

^e Water Quality Center, Trent University, Peterborough, Ontario, Canada

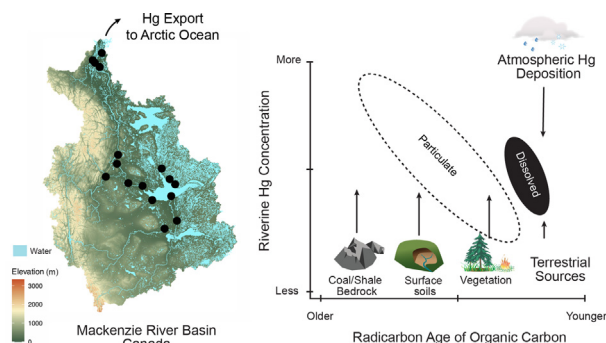
^f Department of Soil and Environment, Swedish University of Agricultural Sciences, Uppsala, Sweden

^g Department of Forest Ecology and Management, Swedish University of Agricultural Sciences, Umeå, Sweden

HIGHLIGHTS

- Sources differ between the particulate and dissolved Hg fractions.
- Dissolved Hg is more strongly associated with atmospheric deposition.
- Particulate Hg is consistently associated with terrestrial sources.
- Riverine Hg concentration are positively correlated with Organic Carbon age.
- River chemistry is strongly contrasted between the Mountain and Lowland area.

GRAPHICAL ABSTRACT



ARTICLE INFO

Article history:

Received 3 August 2021

Received in revised form 30 September 2021

Accepted 1 October 2021

Available online 9 October 2021

Editor: Mae Sexauer Gustin

Keywords:

Mercury
Organic carbon
Stable
Radiocarbon
Fluorescence
Mackenzie River

ABSTRACT

The Arctic environment harbors a complex mosaic of mercury (Hg) and carbon (C) reservoirs, some of which are rapidly destabilizing in response to climate warming. The sources of riverine Hg across the Mackenzie River basin (MRB) are uncertain, which leads to a poor understanding of potential future release. Measurements of dissolved and particulate mercury (DHg, PHg) and carbon (DOC, POC) concentration were performed, along with analyses of Hg stable isotope ratios (incl. $\Delta^{199}\text{Hg}$, $\delta^{202}\text{Hg}$), radiocarbon content ($\Delta^{14}\text{C}$) and optical properties of DOC of river water. Isotopic ratios of Hg revealed a closer association to terrestrial Hg reservoirs for the particulate fraction, while the dissolved fraction was more closely associated with atmospheric deposition sources of shorter turnover time. There was a positive correlation between the $\Delta^{14}\text{C}$ -OC and riverine Hg concentration for both particulate and dissolved fractions, indicating that waters transporting older-OC (^{14}C -depleted) also contained higher levels of Hg. In the dissolved fraction, older DOC was also associated with higher molecular weight, aromaticity and humic content, which are likely associated with higher Hg-binding potential. Riverine PHg concentration increased with turbidity and SO_4 concentration. There were large contrasts in Hg concentration and OC age and quality among the mountain and lowland sectors of the MRB, which likely reflect the spatial distribution of various terrestrial Hg and OC reservoirs, including weathering of sulfate minerals, erosion and extraction of coal deposits, thawing permafrost, forest fires, peatlands, and forests. Results revealed major differences in the sources of particulate and dissolved riverine Hg, but nonetheless a common positive association with older

* Corresponding author.

E-mail address: audrey.campeau@slu.se (A. Campeau).

riverine OC. These findings reveal that a complex mixture of Hg sources, supplied across the MRB, will contribute to future trends in Hg export to the Arctic Ocean under rapid environmental changes.

© 2021 The Authors. Published by Elsevier B.V. This is an open access article under the CC BY license (<http://creativecommons.org/licenses/by/4.0/>).

1. Introduction

Mercury (Hg) is a neurotoxin that accumulates in the Arctic Ocean due to long-range atmospheric transport of anthropogenic emissions from lower latitudes ((AMAP), 2001; Driscoll et al., 2013). This contamination threatens the health of Arctic marine biota, and of local peoples who consume it (Dietz et al., 2013). In the Canadian Arctic, contamination levels in wildlife remains high (Braune et al., 2015), and have even increased in certain species (Castello et al., 2014), despite a global decline in atmospheric Hg concentration. Riverine Hg export currently accounts for ~15–20% of the Hg entering the Arctic Ocean (~41 Mg yr⁻¹) (Dastoor, Submitted; Soerensen et al., 2016). Sources of riverine Hg include atmospheric deposition and runoff, as well as export from terrestrial reservoirs such as surface vegetation, soils and bedrock (Bishop et al., 2020). Permafrost soils in the Arctic and subarctic region store century- to millennia-old Hg. Current estimates suggest that the size of this global reservoir exceeds all others combined (~597 to 809 Gg, (Lim et al., 2020; Schuster et al., 2018)). Permafrost thaw and increasing land-water connectivity due to rapid high-latitude warming in the Arctic may mobilize previously stored terrestrial Hg into aquatic environments (Bishop et al., 2020; Coquery et al., 1995; St Pierre et al., 2018). This could undermine the efficacy of policy efforts imposing limits on global anthropogenic Hg emissions under the Minamata Convention (2017) (Wang et al., 2019), and lead to continued or even increased Hg input to the Arctic Ocean (Schuster et al., 2011; Stern et al., 2012). Identifying the terrestrial sources of riverine Hg among Arctic rivers is thus key to understanding future contamination levels in the Arctic Ocean, and how these may evolve under rapid environmental changes.

The stable isotope ratios (IR) of Hg carry the imprint of transformations and transport processes that regulate the biogeochemical cycling of Hg, thus providing information on its possible sources and entry pathways into riverine systems. Mercury transported in air (e.g., as gaseous elemental Hg), deposited by precipitation (e.g., in snow), or which resides in surface waters for extended periods (e.g., in wetlands) is susceptible to undergo photochemically-induced mass-independent isotopic fractionation (MIF), resulting in recognizable anomalies in the IR of odd-mass isotope, conventionally expressed as $\Delta^{199}\text{Hg}$ or $\Delta^{201}\text{Hg}$ (Bergquist and Blum, 2007). Meanwhile, foliar uptake of Hg(0) is accompanied by mass-dependent fractionation (MDF) favoring lighter isotopes, resulting in negative anomalies in their IR relative to gaseous Hg(0), usually expressed by $\delta^{202}\text{Hg}$ values (Zhou et al., 2021). These anomalies are recognizable in Hg within litterfall and organic soils, and in runoff fed by shallow groundwater circulating in these soils (e.g., in forests; (Demers et al., 2013)). Consequently, Hg IR can be used to discriminate between Hg in streams that is derived from geogenic sources (e.g., bedrock erosion), precipitation or foliar uptake.

Riverine Hg also has a strong affinity for organic carbon (OC), particularly targeting its reduced sulfur sites (i.e. thiol groups) (Haitzer et al., 2002). As a result, DOC and/or TOC concentrations are useful predictors of Hg levels in surface waters worldwide (Lavoie et al., 2019), including in the Arctic region (Coquery et al., 1995; Zolkos et al., 2020). Riverine DOC and Hg concentrations tend to be positively correlated with discharge, indicating common hydrological controls (Brigham et al., 2009; Schuster et al., 2011; Sonke et al., 2018). In recent years, optical properties of dissolved organic matter (DOM), such as UV-Vis absorbance or fluorescence, were found to improve the explanatory power of riverine [DOC] for Hg concentrations (Bravo et al., 2018; Dittman et al., 2009; Eklöf et al., 2012; Grigal, 2003; Lescord et al., 2018).

Meanwhile, the radiocarbon (¹⁴C) content of OC ($\Delta^{14}\text{C-OC}$) can help determine the average age of riverine OC, and help identify key terrestrial pools of both OC and OC-bound Hg in surface waters. Combining Hg IR with measurable properties of DOM/C (such as UV-Vis absorbance and $\Delta^{14}\text{C}$) in streams therefore holds the potential to improve our ability to identify key Hg sources in surface waters and determine how these may vary in the future.

The Mackenzie River is the fourth largest source of freshwater and riverine Hg to the Arctic Ocean (Emmerton et al., 2013; Graydon et al., 2009; Zolkos et al., 2020). During spring freshet, Hg export ranks second among the six largest Arctic rivers (Zolkos et al., 2020). Land-water connectivity in the Mackenzie River Basin (MRB) is changing rapidly due to climate warming. The northernmost part of the Mackenzie River valley has recorded the largest temperature increase in Canada over the past half-century (+3 °C in annual average and +5 °C in winter; (Bush and Flato, 2018)). This is coupled with a local increase in annual precipitation for the same time period (average $15 \pm 13\%$; (Bush and Flato, 2018)) that has contributed to a significant increase in discharge from several rivers within the watershed (Rood et al., 2017). Together, these changes are driving rapid permafrost thaw and river bank slumping, particularly in the northwest sub-basins (e.g. Peel River basin) (Lacelle et al., 2015). Measurable impacts on river chemistry have been observed in recent years, including locally-enhanced OC and Hg transport (Kokelj et al., 2005; St Pierre et al., 2018; Tank et al., 2016), and a shift towards older DOC export (Schwab et al., 2020). Analysis of $\Delta^{14}\text{C-OC}$ across different sub-basins of the MRB revealed a large spatial diversity of terrestrial sources supplying riverine OC (Campeau et al., 2020; Carrie et al., 2009; Hilton et al., 2015). These findings lead to the hypothesis that sources supplying Hg to these rivers may be similarly diverse. The goal of this study was to identify sources of Hg, by investigating links between riverine Hg and OC concentration and properties, as well as patterns in Hg isotopic ratio across the MRB, which in turn may help to better anticipate potential future releases.

2. Material and methods

2.1. Watershed properties and terrestrial reservoirs of Hg

The MRB covers an area of 1.7×10^6 km², making it the largest watershed in Canada. It is marked by east-west elevation contrasts, and straddles three major geological regions. The western sector is comprised of the Cordillera (24% of watershed area) that gives way to the central Interior Plains (54% of watershed area) and, further east, to the lake-dotted landscape of the Canadian Shield (23% of watershed area). Hereafter, the Platform and Shield sectors are referred to as “Lowlands” (mean elevation 428 m.a.s.l and slope 1.4°), to contrast these areas with the much steeper relief of the Cordillera (mean elevation 1187 m.a.s.l and slope 11.1°).

Areas of exposed bedrock are mostly found in the Cordillera and Canadian Shield (Fulton, 2014; Pelletier et al., 2016). Large parts of the MRB are underlain by Phanerozoic sedimentary rocks, including coal and shale deposits, that represent a geological reservoir of both Hg and ancient OC. These are most abundant in the Mackenzie River valley and Cordilleran foreland (e.g. Liard and Peace river basins; (Cameron and Beaton, 2000)), but mostly absent in the eastern sector (Shield), which is mostly composed of gneiss and granitoids. Glacial sediments make up the majority of the surficial deposits across the MRB, and are much thinner in the Canadian Shield (mean depth 10 m) compared with the Interior Platform (mean depth 28 m).

Most of the MRB is located in the boreal forest ecozone. Coniferous forests make up the majority of its landcover. These are interspersed with numerous small lakes and peatlands, especially over the Canadian Shield (Fig. 1). Soil OC and peat accumulation have been ongoing since Late Pleistocene deglaciation, with peatland initiation reaching its peak between 8 and 7 ka BP (Treat and Jones, 2018). Peat-rich soils are most abundant in the Interior platform (Xu et al., 2018). There are three large lakes in the MRB, from south to north; Lake Athabasca, Great Slave Lake and Great Bear Lake (Fig. 1). Permafrost aggradation occurred in the mid- to late Holocene, between ~6–1 ka BP (Treat and Jones, 2018). The watershed contains a north-south gradient of permafrost cover (50% total watershed area), with isolated-sporadic coverage in the southwestern basin, and continuous permafrost in the north. Most permafrost in the Cordillera and Canadian Shield has a thin overburden and a low ice content, while the permafrost areas in the Interior Platform are often under thick overburden and may contain massive ground ice, as for example in the Mackenzie River delta (Brown et al., 2002).

Human influence on rivers of the MRB occur through flow regulation, mining, oil and gas extraction, and agriculture. Large hydropower-generating dams are found on the Peace River (e.g., the W.A.C. Bennett Dam and the Peace Canyon Dam), with

other, smaller dams in the Athabasca and Great Slave Lake sub-basins (e.g., Yellowknife river (Gaur et al., 2019)). Oil and gas extraction can release Hg into waterways or the atmosphere (Nasr et al., 2011). Major operations within the MRB presently occur in the Oil Sands region of the Athabasca sub-basin, while natural gas wells also operate at Norman Wells on the lower Mackenzie River and at Inuvik in the Mackenzie Delta. Many currently-inactive well also exist, as in the Cameron Hills area near the Alberta border. Gold mining, formerly widespread across the Northwest Territories (NWT), has nearly stopped, but many As- and Hg-contaminated sites remain, as for example in Yellowknife. However, these sites only have a local pollution footprint at the scale of the MRB. Agriculture is confined to the southern part of the Interior Platform (Peace and Athabasca sub-basins), comprising 2% of the MRB (Latifovic et al., 2017).

2.2. Water sampling

The river sampling included both spatial (2018) and seasonal (2019–2020) surveys. The spatial survey took place during the spring freshet (8th–30th June), a key period for the riverine export of both Hg and OC to the Arctic Ocean (Raymond et al., 2007; Zolkos et al.,

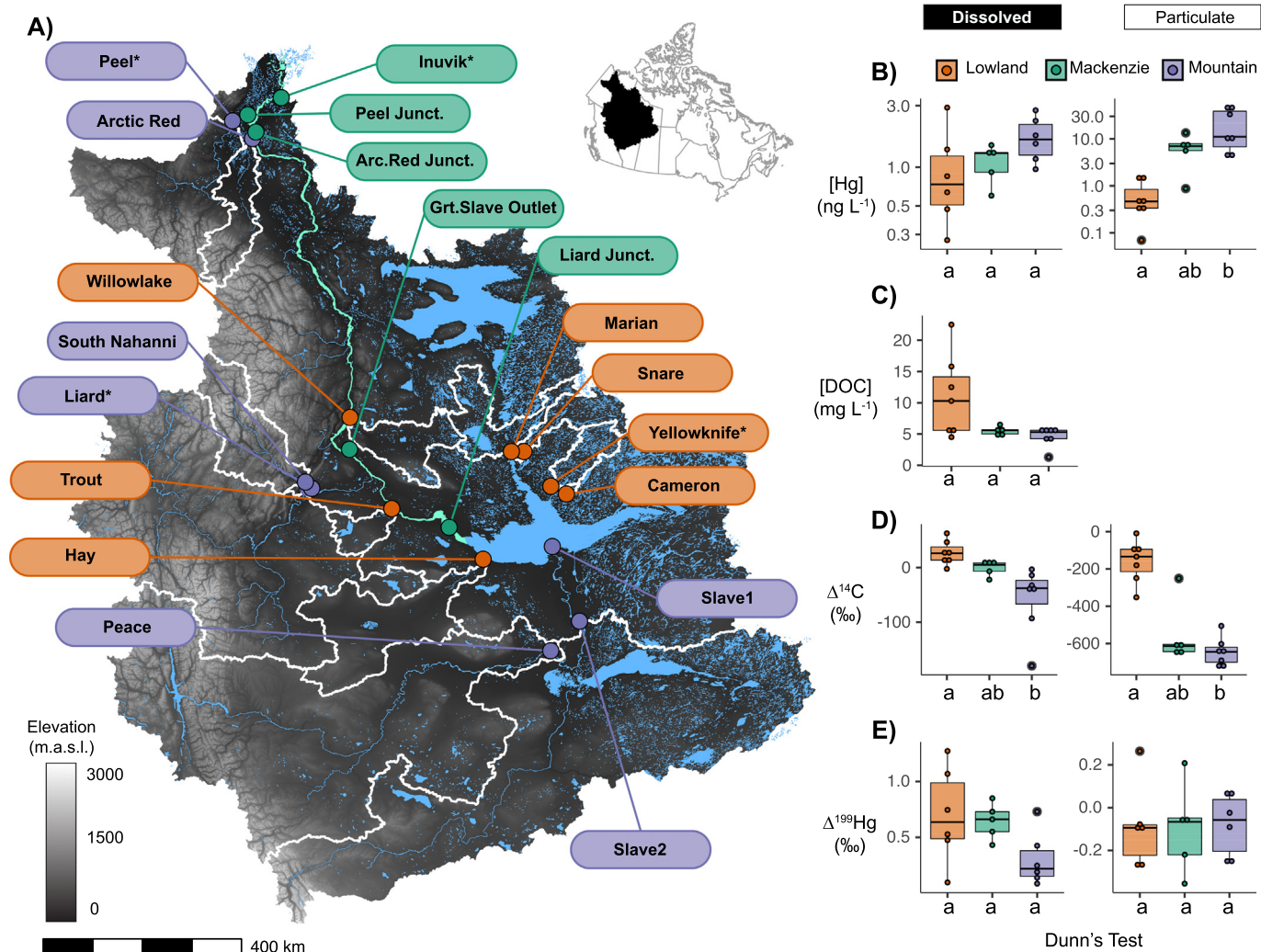


Fig. 1. A) Map of the MRB with elevation displayed in gray shading. Lakes and rivers are colored in blue, with the mainstem of the Mackenzie in light green. Circles indicate each river sampling locations for the spatial survey (June 2018), with the white delineated areas indicating the upstream catchment area for each sampled tributary of the Mackenzie. Circles are colored based on the river category (Lowland tributaries (orange), Mountain tributaries (purple) and Mackenzie main stem (green)) and labeled with the river's name. River names marked with an asterisk were sampled again during the seasonal survey (2019–20). B, C, D, E: Boxplots of [Hg], [OC], $\Delta^{14}\text{C}$ -OC and $\Delta^{199}\text{Hg}$ (‰) for dissolved and particulate fractions in different river categories sampled in the spatial survey. The boxes represent the median, lower, and upper quartiles (25% and 75%) and the whiskers show the 5th and 95th percentiles and results from the Dunn's test are indicated by letters on the x-axis.

2020). This survey included 5 locations along the Mackenzie River itself, and 12 sites on tributaries distributed across all three geological regions (Fig. 1). The catchment area of the surveyed tributaries comprises 62% of the total MRB. Sampling followed the normal progression of seasonal snow melt, beginning south of Great Slave Lake in early June, and ending in the Mackenzie River delta region at the end of the month. As a result, the different rivers were sampled under relatively comparable hydrological conditions with respect to the timing of spring freshet. The seasonal survey included four different rivers, the Peel, Liard, Yellowknife and Mackenzie River that were sampled at four different occasions during the ice-free season of 2019 (June, August, September and October), plus a final sample taken on the Liard River under winter base-flow conditions in March 2020.

Water collection in June 2018 consisted of a single depth-integrated sample from each location. At most sites, samples were collected in mid-channel off a boat's prow. When boat access was unsafe, samples were collected instead in the shallows a few meters off the shore. Depth-integrated samples were collected using suspended sediment samplers models D95 (mid-channel sampling) or D81 (near-shore sampling) (Davis, 2005). Samplers were fitted with an acid-washed 1 L polytetrafluoroethylene (PTFE) bottle, which was rinsed with river water at each site prior to sampling. Water was collected at discrete depth increments of ~1 m (or less in shallower waters), down to just above the channel bed, or to a maximum depth of 5 m. Each 1 L increment sub-sample was poured into a pre-acid-washed, 14-L high-density polyethylene (HDPE) churn (Bel-Art Products, Wayne, NJ, USA). Once back to shore, this composite sample was divided into sub-samples for various water chemistry analyses. Water samples for Hg analyses (concentration and IR) were collected in acid-cleaned 5 L polyethylene terephthalate (PET) carboys (Nalgene Biotainer, Thermo-Fisher Scientific, Waltham, MA USA), while those for $\Delta^{14}\text{C}$ -OC analyses were taken in sterile 1 L HDPE bottles. Sampling in 2019–20 was carried out by partners in local communities of the NWT. These samples were collected from surface water only, either from a boat (Yellowknife, Peele and Mackenzie River) or from near shore (Liard River), using the same types of containers as in 2018. Additional details on the field water sampling procedure are provided supplementary material and method Section 1.

2.3. Basic water properties

A set of basic physical and chemical properties were measured in water samples at Taiga Environmental Laboratory, operated in Yellowknife by the NWT Government's Department of Environment and Natural Resources. Among the parameters measured were pH, specific conductance (SC), turbidity, total dissolved solids (TDS), total suspended solids (TSD), alkalinity, as well as concentrations of DOC ([DOC]) and of six major ionic species (Ca^{2+} , K^+ , Na^+ , Mg^{2+} and SO_4^{2-}). The [DOC] was measured on a Shimadzu TOC/DOC analyzer, and major ions on a Thermo Fisher Dionex ICS 5000 ion chromatography system. Particulate organic carbon concentration [POC] was derived from the difference between [TOC] and [DOC] concentration. However, these data are highly uncertain due to potential sedimentation of particles at the bottom of the vials during sample processing. About 40% of the resulting estimates of [POC] were found below the detection limit. All measurements of basic water properties were performed as per standard US Environmental Protection Agency (EPA) methods or the Standard Methods for the Examination of Water and Wastewater (Rice et al., 2017).

2.4. Mercury analyses

Water for Hg analyses was filtered through quartz microfiber filters (Pall Tissuequartz 2500 QAT-UP, Pall Corporation, Port Washington, NY, USA), and DHg and PHg (filtered particulates) were analyzed separately at the Department of Chemistry of Trent University, Canada. Filtered

water aliquots were digested with 0.2 M BrCl for at least 12 h and DHg concentrations ([DHg]) were determined by Cold-Vapor Atomic Fluorescence Spectroscopy (CV-AFS) on a Tekran 2600 instrument (Tekran® Instruments Corporation, CA) following U.S. EPA Method 1631E, with a precision better than 10% (RSD for the slope of the calibration curve). Concentrations of PHg in water ([PHg]; m/v ratio) were calculated from Hg concentrations and the mass of filtered particulate matter for a set volume of filtered water. Filters were stored frozen at $-20\text{ }^\circ\text{C}$, then freeze-dried, placed in quartz tubes, and the particle-bound Hg was released by combustion (Huang et al., 2015). The volatilized Hg was trapped in an oxidizing solution and quantified as described above for water samples.

The Hg IR were determined on a Nu II Multi-Collector Inductively-Coupled Mass Spectrometer (MC-ICP-MS; Nu Instruments Ltd., UK) following established methods (Blum and Bergquist, 2007; Chen et al., 2012). Instrumental bias was corrected using the addition of an internal standard (NIST SRM 997 with $^{205}\text{Tl}/^{203}\text{Tl}$ ratio of 2.38714) and sample standard bracketing (SSB) with NIST SRM 3133 Hg standard. The Hg IR (MDF) are reported as delta values in per-mil (‰) relative to the average ratios measured in NIST SRM 3133 following:

$$\Delta^{\text{xxx}}\text{Hg} = \left[\left(\frac{{}^{\text{xxx}}\text{Hg}/{}^{198}\text{Hg}}{\text{sample}} / \left(\frac{{}^{\text{xxx}}\text{Hg}/{}^{198}\text{Hg}}{\text{SRM 3133}} \right) - 1 \right] \times 1000$$

where xxx = 199, 200, 201, 202. The MIF of Hg isotopes is expressed as the difference (Δ) between measured and theoretically predicted values of $\delta^{\text{xxx}}\text{Hg}$ (assuming MDF only), approximated as

$$\Delta^{\text{xxx}}\text{Hg} = \delta^{\text{xxx}}\text{Hg}_{\text{sample}} - \left(\delta^{202}\text{Hg}_{\text{sample}} \times \alpha_{\text{xxx}} \right)$$

where α_{xxx} is the appropriate kinetic or equilibrium fractionation factor (Blum and Bergquist, 2007). Repeated measurements of the NIST SRM 8610 (UM-Almadén) Hg agreed with the previous studies (Blum and Bergquist, 2007) and gave long-term average values of -0.54 ± 0.06 , -0.02 ± 0.07 , 0.02 ± 0.07 , -0.02 ± 0.09 and $0.02 \pm 0.09\text{‰}$ for $\delta^{202}\text{Hg}$, $\Delta^{199}\text{Hg}$, $\Delta^{200}\text{Hg}$, $\Delta^{201}\text{Hg}$ and $\Delta^{204}\text{Hg}$ (2σ , $n = 16$), respectively.

Almost all samples for Hg analysis collected during the spatial survey (2018) were filtered on-site immediately after sample collection, with the exception of two samples with excessive particle load (i.e. the Arctic Red River and Peel River), which were filtered in the lab approx. 12 months after collection. Samples collected during the seasonal survey (2019–2020), were shipped unfiltered to the laboratory, and filtration was performed 8–40 days later. Redistribution of Hg across the dissolved and particulate phase in water samples during storage is possible (Guevara and Horvat, 2013). However, results from the Hg IR analysis indicate a persistent separation between the DHg and PHg phase, with no evidence of converging Hg IR in samples with delayed filtration. While this does not constitute direct proof that storage has no effect on DHg/PHg distribution, it indicates that potential changes had no significant impact on the Hg measurements. Further details on the procedure for riverine Hg concentration and IR analysis are provided supplementary material and method Section 2.

2.5. Dissolved organic matter optical properties

Optical characterization of dissolved organic matter (DOM) was done by UV-Visible absorbance and fluorescence spectroscopy. Samples were filtered with glass microfiber filters (GF/F, Whatman) upon arrival to the laboratory at the Department of Aquatic Science and Assessment at the Swedish University of Agricultural Sciences. UV-Vis absorbance spectra between 240 nm to 600 nm and with 2 nm resolution were measured on a Horriba Aqualog spectrophotometer that measures simultaneously absorbance and fluorescence. A quartz cuvette with a path length of 1 cm was used. The UV absorbance at 254 nm was also measured using an Avantes AvaSpec-ULS3648 high resolution spectrometer. Fluorescence and absorbance data were analyzed in Matlab

using custom-build functions for scatter removal (Bieroza and Heathwaite, 2016) and Raman normalization (Lawaetz and Stedmon, 2009). To retrieve the fluorescence and absorbance information, a number of parameters were calculated. The fluorescence index (FIX) (McKnight et al., 2001) is used to distinguish sources of fulvic acids, with values below 1.4 being typical for terrestrial material and values above 1.9 typical for microbially-derived fulvic acids. The humification index (HIX) measures the degree of DOM humification by comparing total fluorescence intensity at longer (435–480 nm) and shorter (300–345 nm) emission wavelengths (Ohno, 2002). Specific ultraviolet absorbance ($SUVA_{\text{abs}254}$) was calculated as absorbance 254 nm divided by the [DOC]. Spectral slope (SSratio) was calculated over wavelength intervals (275–295 nm, 350–400 nm) that is sensitive to changes in DOC molecular weight (Helms et al., 2008). The ratio of absorption at 250 to 365 nm (called E2/E3) was used to track changes in the relative size of DOM molecules (De Haan and De Boer, 1987). Both the Ssratio and E2/E3 are inversely related to the DOM molecular weight.

2.6. Carbon isotopes

For analysis of the $\Delta^{14}\text{C}$ -content of DOC and POC, sub-samples of water were filtered through quartz microfiber filters (Whatman grade QM-A, GE Healthcare, Chicago, IL, USA) which had been pre-baked at 500 °C and treated with HCl to remove volatile organics and carbonates. Determination of $\Delta^{14}\text{C}$ was performed at the A. E. Lalonde Accelerator Mass Spectrometry Laboratory of the University of Ottawa (Crann et al., 2017; St-Jean et al., 2017). Sample pre-treatment to remove inorganic carbon from carbonates was done with HCl for POC, and with H_3PO_4 for DOC, following a wet oxidation technique (Lang et al., 2016; Zhou et al., 2015). The CO_2 evolved from DOC or POC was then cryogenically purified on a vacuum extraction line, and the $^{14}\text{C}/^{12}\text{C}$ ratio in CO_2 was determined on a 3MV tandem accelerator mass spectrometer (High Voltage Engineering, Amersfoort, the Netherlands). Three blank quartz filters with known masses of ^{14}C -free acetanilide were analyzed along with samples, and the released carbon mass (mC) and $\Delta^{14}\text{C}$ on these were used to correct the sample $\Delta^{14}\text{C}$ values using a mass balance method (Roberts et al., 2019). Total analytical uncertainties (2σ) on individual $\Delta^{14}\text{C}$ values ranged between 1.88 and 6.38‰ (median 3.95‰), which correspond to relative uncertainties of 0.3–6.0%, with the exception of a single sample (NT18-1; Cameron River), in which the uncertainty was much larger (43.8%) owing to its low OC content. Results are reported here as $\Delta^{14}\text{C}$ values in ‰, which expresses the relative difference in ^{14}C activity between the absolute international standard (base year 1950) and the sample activity corrected for age and normalized to $\delta^{13}\text{C} = 25\%$ (Stuiver and Polach, 1977). More detailed methods can be found in (Campeau et al., 2020).

2.7. Geospatial and statistical analysis

The upstream catchment area of each sampling location was determined using the hydrology toolbox on ArcGIS 10.7. These areas were computed from the void-filled Canadian digital elevation model (CDEM; <http://ftp.geogratis.gc.ca>), with a spatial resolution of 100 m², following aggregation of the original 20 m² resolution data. Stream lines were drawn using a 1 km² threshold on the derived flow accumulation raster. Soil thickness and peatland coverage were determined for each sub-basins according to (Xu et al., 2018), and (Pelletier et al., 2016), respectively. Tributaries of the Mackenzie Rivers and rivers feeding into Great Slave Lake were separated into two groups. The “Mountain” group included those with their headwaters in the Cordillera (i.e. Slave, Peace, Liard, Arctic Red and Peel), while the “Lowland” group included those with their headwaters in the Canadian Shield (i.e. Cameron, Snare, Yellowknife) or the Interior Platform (i.e. Hay, Trout, Willowlake).

All subsequent data analyses, as well as figures, were made using R (R Core Team, 2020) using specific commands and packages including

raster, *sp*, *sf*, *rgdal* and the *tidyverse* (Wickham et al., 2019). The non-parametric Spearman coefficient was computed to identify statistically significant correlations ($p > 0.05$) between water chemistry variables, while significant differences between river groups were identified with Kruskal-Wallis one-way ANOVA non-parametric tests, and stochastic dominance with Dunn's test. A major axis linear regression model II was used to determine the relationship between $\Delta^{199}\text{Hg}$ and $\Delta^{201}\text{Hg}$ (package *lmodel2*). The confidence intervals (2.5% and 97.5%) for the slope and intercept estimation are presented in brackets in the main text. Principal component analysis (PCA) was performed to summarize co-linearity between 16 different water chemistry variables and 4 watershed properties. Calculations were made by singular value decomposition of the centered and scaled correlation matrix with non-transformed variables (function *prcomp*). One-way ANOVA tests were performed to compare the variance within (seasonal survey) and across sites (spatial survey).

3. Results and discussion

3.1. Riverine Hg concentration and stable isotope ratio

Riverine [Hg] varied across one order of magnitude for the dissolved fraction ([DHg], 0.3 to 2.9 ng L⁻¹) and close to three orders of magnitude for the particulate fraction ([PHg], 0.07 to 47.4 ng L⁻¹) in the spatial survey conducted in the spring of 2018 (Fig. 1B). The particulate fraction corresponded on average to 40% of the total riverine Hg pool in the Lowland tributaries, which was significantly lower than for the Mountain tributaries and Mackenzie River (75% and 77%). The importance of [PHg] for the riverine Hg pool was also demonstrated in other studies (Leitch et al., 2007; St Pierre et al., 2018). The median [PHg] was significantly lower in the tributaries of the Lowland region compared with the Mountain tributaries, where the highest median [DHg] and [PHg] occurred (Fig. 1B). This is again consistent with published data from the region (Emmerton et al., 2013; Leitch et al., 2007; Schuster et al., 2011). The patterns in [DHg] between groups of rivers were similar to those of [PHg] but were not statistically significant (Fig. 1B). There were also no statistically significant differences between the median $\Delta^{199}\text{Hg}$ or $\delta^{202}\text{Hg}$ values across the different categories of rivers, for neither PHg or DHg fractions ($\Delta^{199}\text{DHg } p = 0.09$, $\Delta^{199}\text{PHg } p = 0.8$ (Fig. 1E), $\delta^{202}\text{PHg } p = 0.5$, $\delta^{202}\text{DHg } p = 0.7$).

The spatial survey revealed that the DHg and PHg fractions are characterized by distinct isotope ratios. The $\delta^{202}\text{DHg}$ was significantly more positive than the $\delta^{202}\text{PHg}$ values ($p = 0.0004$, $\delta^{202}\text{DHg}$ varied from -1.77‰ to +0.15‰ and $\delta^{202}\text{PHg}$ from -2.12‰ to -1.55‰, Fig. 2). This was also the case for the $\Delta^{199}\text{Hg}$ values, which was also significantly more positive in the dissolved than in the particulate fraction ($p < 0.0001$, $\Delta^{199}\text{DHg}$ ranged from +0.09‰ to +1.27‰ and $\Delta^{199}\text{PHg}$ from -0.36‰ to +0.26‰, Fig. 2). The distinct IRs of DHg and PHg suggests that these two fractions of the riverine Hg pool are not at equilibrium. While there have been reports that Hg isotopes fractionate during absorption or complexation process, the associated fractionation factors are too small to account for the differences observed in this study (Wiederhold et al., 2010). Riverine DHg and PHg appear to stem, at least partly, from different sources. The majority of MIF values for PHg were negative, and only a few were positive (Fig. 2A). This is in contrast to DHg, where almost all MIF values were significantly larger than zero (Fig. 2A). Typically, Hg in precipitation has MIF values $>0\%$, consistent with most DHg IR in our river samples. On the other hand, gaseous Hg that is absorbed into foliage and subsequently enters the watershed through litterfall often exhibits very negative MDF values (Demers et al., 2013; Jiskra et al., 2015), consistent with the observed PHg IR in these samples.

The differences in Hg sources between the dissolved and particulate fractions are also emphasized by $\Delta^{201}\text{Hg}/\Delta^{199}\text{Hg}$ linear regression analysis. The $\Delta^{201}\text{Hg}/\Delta^{199}\text{Hg}$ relationship is often used to decipher the underlying processes controlling MIF in a given system (Chen et al.,

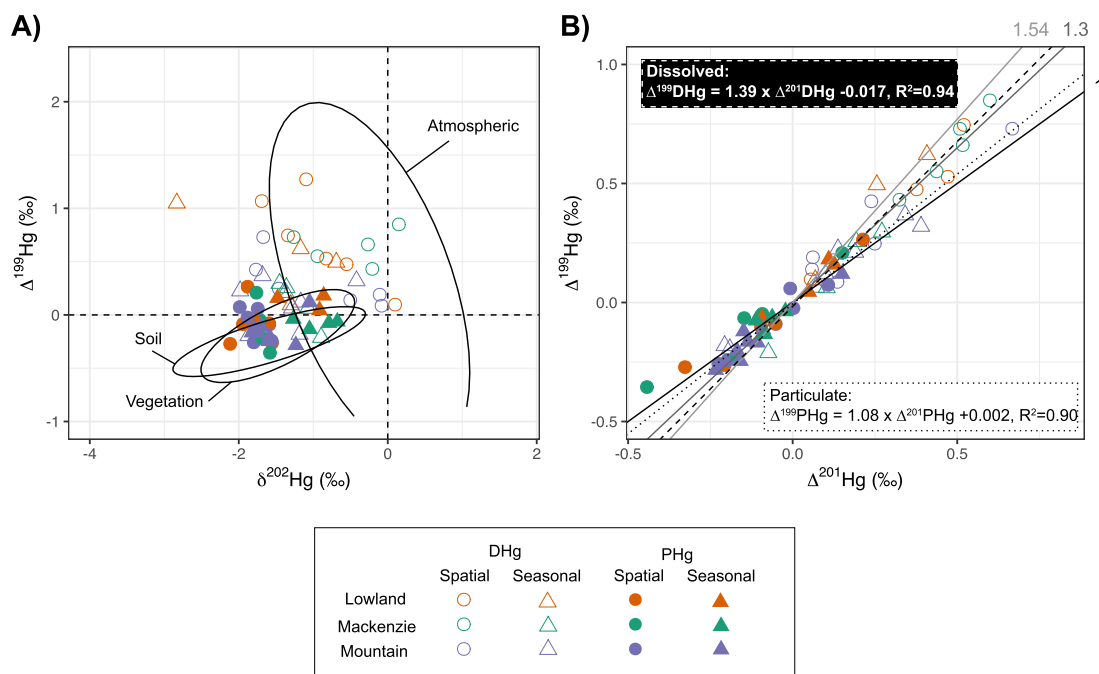


Fig. 2. Scatterplots of $\Delta^{199}\text{Hg}$ against A) $\delta^{202}\text{Hg}$ and B) $\Delta^{201}\text{Hg}$, each in (‰), for all river samples (including spatial and seasonal survey). Symbols are colored by their category (Lowland (orange), Mountain (purple), Mackenzie (green)). Open and closed symbols represent the DHg and PHg fraction, respectively. The circles and triangles represent the samples collected during the 2018 spring spatial survey and the 2019–20 seasonal survey, respectively. In A) the end-members for key Hg sources for this region are identified in the black ellipses, based on published data presented in detail in supplementary file (Fig. S4 and Table S3). In B) the dashed and dotted lines represent the major axis linear model regression two for the dissolved and particulate fraction, respectively. The full lines in shades of gray indicate different key transformation processes: in black, slope = 1 which is typical of photo reduction of inorganic Hg, in gray, slope = 1.3 that is representative of photodemethylation of monomethylmercury, in light gray, slope = 1.54, which is representative of evaporation of elemental Hg.

2016). Empirical evidence suggests that slopes of 1.36 are produced by photodemethylation of monomethylmercury (MMHg) (Bergquist and Blum, 2007), while photoreduction of inorganic Hg typically results in slopes of 1.0, although values of up to 1.3 have been generated in laboratory experiments (Zheng et al., 2018). Fractionation processes controlled by nuclear volume effects (NVE), such as evaporation of elemental Hg or chemical reduction in the absence of light, lead to slopes of 1.54 (Zheng and Hintelmann, 2010).

The $\Delta^{201}\text{Hg}/\Delta^{199}\text{Hg}$ in DHg from both the spatial and the seasonal surveys displayed a slope of 1.39 (C.I. 1.27 to 1.52) with an intercept of -0.017 (C.I. -0.055 to -0.018). In comparison, the $\Delta^{201}\text{Hg}/\Delta^{199}\text{Hg}$ slope for PHg is only 1.08 (C.I. 0.96 to 1.21) which is not significantly different from 1.0, with an intercept of 0.002 (C.I. -0.007 to 0.012). Generally, $\Delta^{201}\text{Hg}/\Delta^{199}\text{Hg}$ ratios found in this study are larger than those reported for terrestrial or atmospheric samples, and are therefore likely caused by more than a single process or source (Fig. 2). Observed values might be explained by multicomponent mixing models, whereby already photoreduced Hg (II) from precipitation is further fractionated in river water after photoreduction and re-emission to the atmosphere. This could lead to the observed slope of 1.35 for DHg that lies between MIF ratios expected for photoreduction (1.0) or evasion (1.54). As well, the measurements were based on total Hg (THg) measurements. THg could therefore also include dissolved MMHg, which may have been subjected to photodemethylation. This should result in a slope of 1.36, if all DHg was in fact MMHg. While MMHg was not determined in this study, between 0.2 and 9% of Hg in the Mackenzie and Yukon rivers have been reported to be present in the form of MMHg (Emmerton et al., 2013; Schuster et al., 2011).

The range of possible $\Delta^{201}\text{Hg}/\Delta^{199}\text{Hg}$ ratios illustrated on Fig. 2B assume a starting point of $-0.6\text{‰}/-0.6\text{‰}$, which is commonly observed in abiotic samples. If this were the initial MIF for DHg, the three lines representing the individual fractionation processes enclose most of the observed values in these rivers, suggesting that a combination of fractionation processes is in fact required to explain the values recorded

here. Choosing different starting points would result in slightly different enclosing areas, but still encompass all measured data. Since final MIF values are likely the result of at least 3 different fractionation processes, this approach cannot identify individual contributions. As well, other starting points would require different proportions for each process to account for the final MIF.

Hg IR suggest that the dissolved fraction was affected by photoreduction of inorganic Hg, hence ultimately connected to atmospheric reservoirs (Fig. 2). Most likely, the majority of DHg during the spring flood arises from precipitation and snowmelt runoff (Fig. 2). In comparison, the magnitude of fractionation found in PHg is small, supporting the idea that this Hg is from terrestrial sources, where photoreactions are not important (Demers et al., 2013; Jiskra et al., 2015; Obrist et al., 2017). PHg IR indicate a consistent association with terrestrial sources, which only infrequently resembles Hg signatures found in precipitation. The PHg fraction is therefore more closely associated with surface vegetation and soil, of potentially longer turnover time than DHg. Data collected in this study suggest that Hg source tracing through IR in the MRB is complicated by mixing of different sources. Localized geogenic sources (e.g., shales) do not dominate individual rivers, and overall signatures are reflective of erosion and overland flow. Future studies identifying riverine Hg sources must consider separate analysis of DPg and PHg. This study shows that the two fractions can be dominated by very different sources. Bulk analysis of water samples would obscure the individual contributions and may lead to misinterpretations.

3.2. Correlations between riverine [Hg] and $\Delta^{14}\text{C}$ -OC

Arctic rivers act as conduits of both terrestrial Hg and OC to the Arctic Ocean. (Soerensen et al., 2016; Stein and Macdonald, 2004; Zolkos et al., 2020). Terrestrial Hg and OC reservoirs include forest and tundra vegetation, catchment soils and the underlying bedrock (Bishop et al., 2020). The age of Hg and OC stored in these reservoirs can thus span from days

to millennia and geological timescales. Riverine [Hg] are typically positively correlated with [DOC] (Lavoie et al., 2019). However, the spatial survey across the MRB (Fig. 1) showed no such correlation between [DOC] and [DHg] ($\rho = 0.28$, $p = 0.3$) (Fig. 2, Fig. S5). A study conducted along the mainstem of the Mackenzie river also reported a poor coupling between [DOC] and [Hg] (Leitch et al., 2007). In the neighboring Yukon river, however, the typical positive correlation between [Hg] and [DOC] prevails (Schuster et al., 2011). Yet, a rather poor coupling between [DOC] and [Hg] is also apparent over seasonal timescale at the mouth of the six Arctic Great Rivers, including both the Mackenzie and Yukon River ($p = 0.09$ (Zolkos et al., 2020)).

The spatial survey revealed instead a significant negative correlation between $\Delta^{14}\text{C}$ -DOC and [DHg] ($\rho = -0.55$, $p = 0.02$, Fig. 3A), and between $\Delta^{14}\text{C}$ -POC and [PHg] ($\rho = -0.86$, $p < 0.0001$, Fig. 3B) across the MRB during spring flood. This correlation indicated that rivers transporting more ^{14}C -depleted (i.e. older) OC also contained higher [DHg] and [PHg], irrespective of the [OC] (Fig. 3). Riverine [Hg] therefore correlates more with the source (mean age) of OC than its amount, indicating a more direct association with molecules of aged OC rather than with the bulk OC pool. To our knowledge, no former study has established a link between [Hg] and $\Delta^{14}\text{C}$ -OC in surface waters before. The correlations between [Hg] and $\Delta^{14}\text{C}$ were consistent for both the dissolved and particulate fractions, despite major differences in their sources determined by IR inferences (Fig. 2). There was no statistically significant relationship between the $\Delta^{199}\text{Hg}$ or $\delta^{202}\text{Hg}$ and $\Delta^{14}\text{C}$ -OC ($p > 0.2$) (Fig. 4). However, the differences in DHg and PHg sources inferred from the Hg IR (i.e. DHg was more closely associated with recent atmospheric deposition, while PHg arises from slower turnover terrestrial sources), were also reflected in the gap in ^{14}C -content between DOC and POC (i.e. younger DOC compared with POC).

3.3. Correlations between [DHg] and DOC quality

Correlations between [DHg] and UV fluorescence characteristics of DOM provided further insights into the underlying association between [DHg] and $\Delta^{14}\text{C}$ -DOC at a molecular level. There were multiple significant correlations between [DHg] and optical properties of DOM, including; $\text{SUVA}_{\text{abs}254}$ ($\rho = 0.75$, $p = 0.0009$), E2:E3 ratio ($\rho = -0.74$, $p = 0.0007$), HIX ($\rho = 0.61$, $p = 0.01$), SSratio ($\rho = 0.67$, $p = 0.003$) and FreshIX ($\rho = 0.52$, $p = 0.03$), which were themselves closely correlated ($\rho > 0.9$, $p < 0.0001$) (Fig. 3). Rivers with higher [DHg] thus transported more aromatic DOM ($\text{SUVA}_{\text{abs}254}$), with a higher degree of humification (HIX) and higher molecular weight (lower E2/E3 ratio and SSratio) (Fig. 3). At a molecular level, DOM with higher molecular weight, aromaticity and humic acid content may contain more reduced sulfur sites, making it a better vessel for transporting recently deposited Hg to surface waters (Haitzer et al., 2002; Skjyllberg et al., 2006). At the landscape level, both DHg and ^{14}C -depleted DOC with higher aromaticity, humic content and molecular weight, could also co-vary among the tributaries of the Mackenzie due to a common sourcing from variable terrestrial reservoirs.

Among the different optical properties of DOM, $\text{SUVA}_{\text{abs}254}$ was the strongest variable correlating with riverine [DHg] (Fig. 3). This adds to an existing body of research having reported positive relationships between [Hg] and $\text{SUVA}_{\text{abs}254}$ or total absorbance at 254 nm in surface waters. (Bravo et al., 2018; Dittman et al., 2009; Eklof et al., 2012; Grigal, 2003; Lescord et al., 2018) However, most of these studies also report a co-existing positive correlation between [DOC] and [Hg] in the same waters. In these studies, $\text{SUVA}_{\text{abs}254}$ improved the predictability of riverine [DHg] over an existing relationship with the bulk DOC (Lavoie et al., 2019). This differs from the MRB, where [DOC] is not significantly correlated with its optical properties ($p > 0.05$), $\Delta^{14}\text{C}$, or [DHg] (Fig. 3). Remote sensing methodologies have the capacity to quantify $\text{SUVA}_{\text{abs}254}$ in surface waters (Griffin et al., 2018), which may provide useful monitoring systems for riverine [DHg] across the MRB.

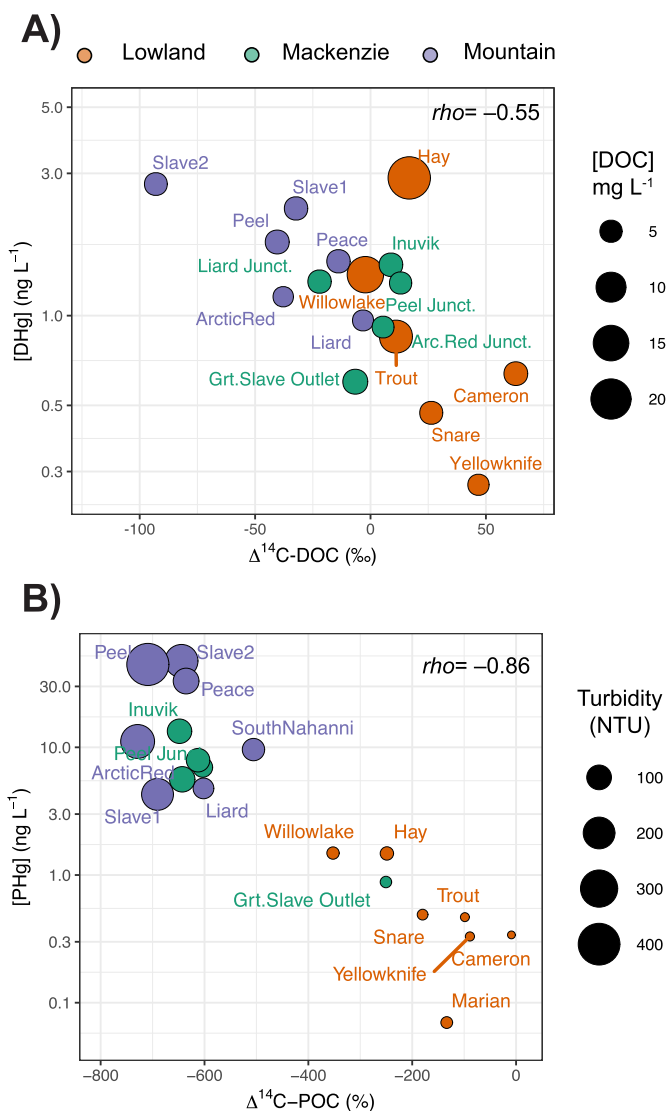


Fig. 3. Scatterplot of [Hg] (ng L^{-1}), on logarithmic scale, as a function of the $\Delta^{14}\text{C}$ -OC (‰) in the A) dissolved and B) particulate fraction. Circles are colored by their category (Lowland (orange), Mountain (purple), Mackenzie (green)), with circle sizes proportional to A) the DOC concentrations (mg C L^{-1}) in and B) Turbidity (NTU). Each circle is labeled by the river's name as indicated on the map in Fig. 1.

A significant positive correlation between [DHg] and [DOC] and $\text{SUVA}_{\text{abs}254}$ emerged when considering only the subset of 6 rivers associated with the Lowland region (Fig. S6). The interplay between [DHg] and [DOC] and quality in this region seems to agree better with the relationships established in the literature (Lavoie et al., 2019). The landscape of the Canadian shield and Interior platform, forming together the lowland of the MRB, is more comparable to other parts of Canada and Fennoscandia where much of the former research has been conducted (Dittman et al., 2009; Eklof et al., 2012; Lescord et al., 2018). The other sectors of the MRB, where other types of terrestrial DOC and Hg sources are present (e.g. thawing permafrost, coal deposits and Hg-bearing sediments) possibly make this catchment deviate from the formerly established patterns.

3.4. Correlations between [PHg] and Turbidity and $[\text{SO}_4^{2-}]$

The negative correlation between [PHg] and $\Delta^{14}\text{C}$ -POC also corresponded with a positive correlation between [PHg] and turbidity

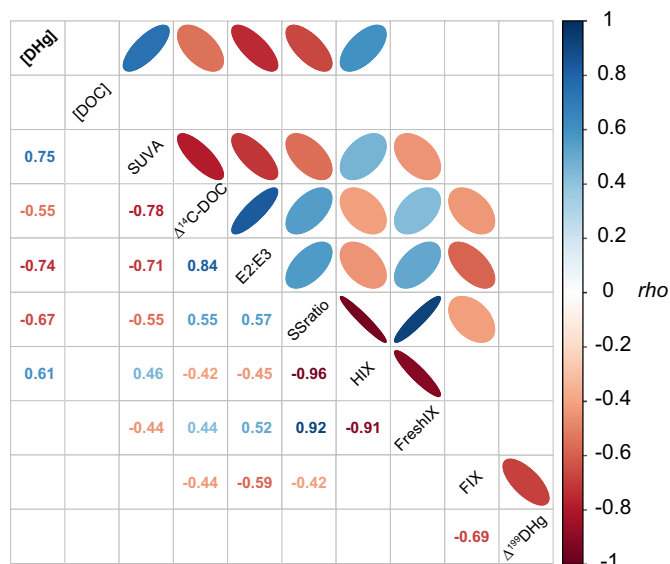


Fig. 4. Spearman correlation matrix of [DHg], [DOC] and various properties of DOC, incl. $\Delta^{14}\text{C}$ -content and optical properties, as well as $\Delta^{199}\text{DHg}$ values for samples collected during the spatial survey ($n = 17$). The top half of the plot shows ellipses scaled to the Spearman correlation coefficient (ρ), while the values of the coefficients are shown in the bottom half. The orientation and colour of the ellipses indicate negative (red) and positive (blue) correlations (ρ scale on right-hand side). Boxes with non-significant correlations ($p < 0.05$) are blanked.

($\rho = 0.88$ $p < 0.0001$) (Fig. 3, Fig. S7A). In the MRB, more turbid waters contain both higher [PHg] and more $\Delta^{14}\text{C}$ -depleted POC (Campeau et al., 2020) (Fig. 3). Turbidity is generally well correlated with total suspended solid concentration, which earlier studies identified as a key predictor of [Hg] in the Mackenzie River (Emmertson et al., 2013; Leitch et al., 2007; Zolkos et al., 2020) and in other Arctic rivers (Vermilyea et al., 2017). In the Mackenzie River, turbidity also correlates strongly with [POC] (Emmertson et al., 2013; Holmes et al., 2018) suggesting a potential positive correlation between [PHg] and [POC], which unfortunately cannot be directly assessed with this dataset.

River turbidity can also be measured using remote sensing methodologies (Kuhn et al., 2019), which could potentially facilitate large-scale monitoring of [PHg] across the MRB. Erosion and weathering of catchment soils are an important source of turbidity in rivers, which is consistent with the importance of terrestrial Hg sources inferred from the PHg IR (Fig. 2). A contribution from erosion and weathering of coal, shales or sulfide minerals in the Mackenzie Mountains is also likely (Carrie et al., 2009; Zolkos et al., 2018), but these are localized sources and unlikely to dominate the signature of the entire river catchment. The positive correlation between [PHg] and $[\text{SO}_4^{2-}]$ among the different sub-catchments ($\rho = 0.68$ $p = 0.001$) supports a link between weathering of sulfide bearing minerals in riverbank sediments and erosion of coal deposits, at least in some tributaries (Fig. 3, Fig. S7B).

3.5. Spatial distribution of terrestrial Hg and OC sources across the MRB

The PCA discriminated between rivers from different geographical regions (i.e. Mountain, Lowland, Mackenzie), with the first two axis accounting for 72% of the total variance within the spatial survey dataset ($n = 17$) (Fig. 5). Previous studies conducted on riverbank sediments along the Mackenzie's mainstem also reported significant differences in [Hg] among the mountain and lowland sectors of the basin (Carrie et al., 2009; Carrie et al., 2012). The Mackenzie River cluster was centered around the intercept of the two PCA axes, which is coherent with a mixture of water chemistry representative of its different tributaries (Fig. 5).

The Mountain rivers contained significantly higher [Hg] and older OC (most ^{14}C -depleted) than the Lowland rivers (Fig. 1B, D), despite having relatively similar [OC] (Fig. 1C). In the PCA, the Mountain rivers projected positively with turbidity, [PHg], $[\text{SO}_4^{2-}]$, $[\text{Mg}^{2+}]$ and mean watershed slope (Fig. 5). The Mountains contain pyrite bearing rocks, as well as exposed or shallow coal deposits, which both contain Hg and geological OC. The steeper elevation and higher precipitation regime in the Mountains may promote erosion and weathering. These likely contribute to the river's higher turbidity, mineral content, and older-POC along with higher [Hg]. Analyses of riverbank sediments along the Mackenzie river indicated that weathering of sulfide minerals and erosion of coal deposit were important Hg sources for the Mountain rivers (78% and 10% respectively; (Carrie et al., 2012)), which appears

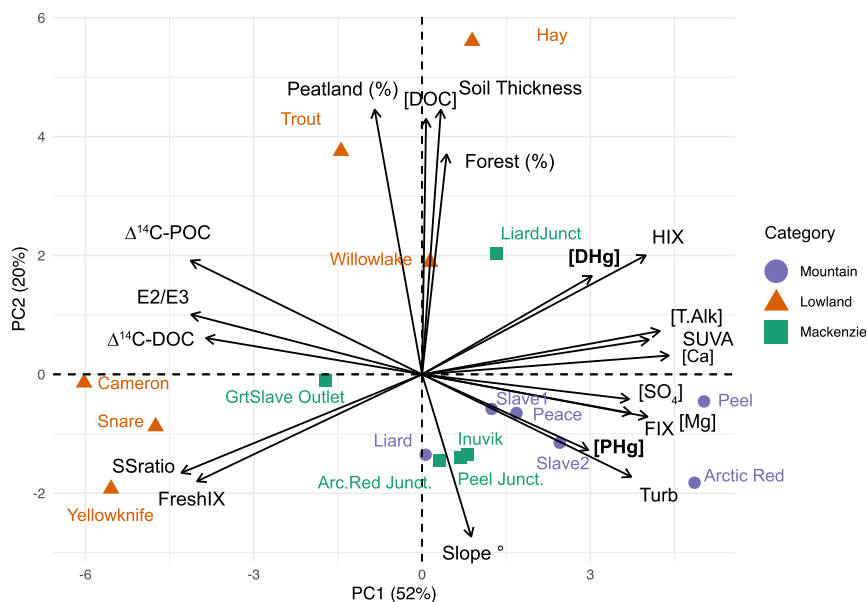


Fig. 5. Bi-plot of the principal component analysis of the water chemistry variables measured during the spring spatial survey in the MRB ($n = 17$) with first and second axes plotted. Symbols represent the score plot, identifying different river sample location grouped by Mountain tributaries (purple circles), Lowland tributaries (orange triangles) and the Mackenzie River (green squares). Each symbol is labeled by the river's name. Arrows represent the loading plot, where vectors identify different water chemistry variables projected on the two dimensions of the principal component.

consistent with the suspended riverine chemistry observed in these data.

The Peel River transported some of the highest [DHg] and [PHg] along with some of the most ^{14}C -depleted DOC and POC (Fig. 2). This was also confirmed during the seasonal survey, which revealed

sustained high [PHg] together with a low $\Delta^{14}\text{C}$ -POC during the summer months compared with the spring flood (Fig. 6D). This catchment is heavily affected by retrogressive thaw slumps (Lacelle et al., 2015), a geomorphological phenomenon that increases the mobilization of ancient OC and Hg stocks (St Pierre et al., 2018). In recent years, such

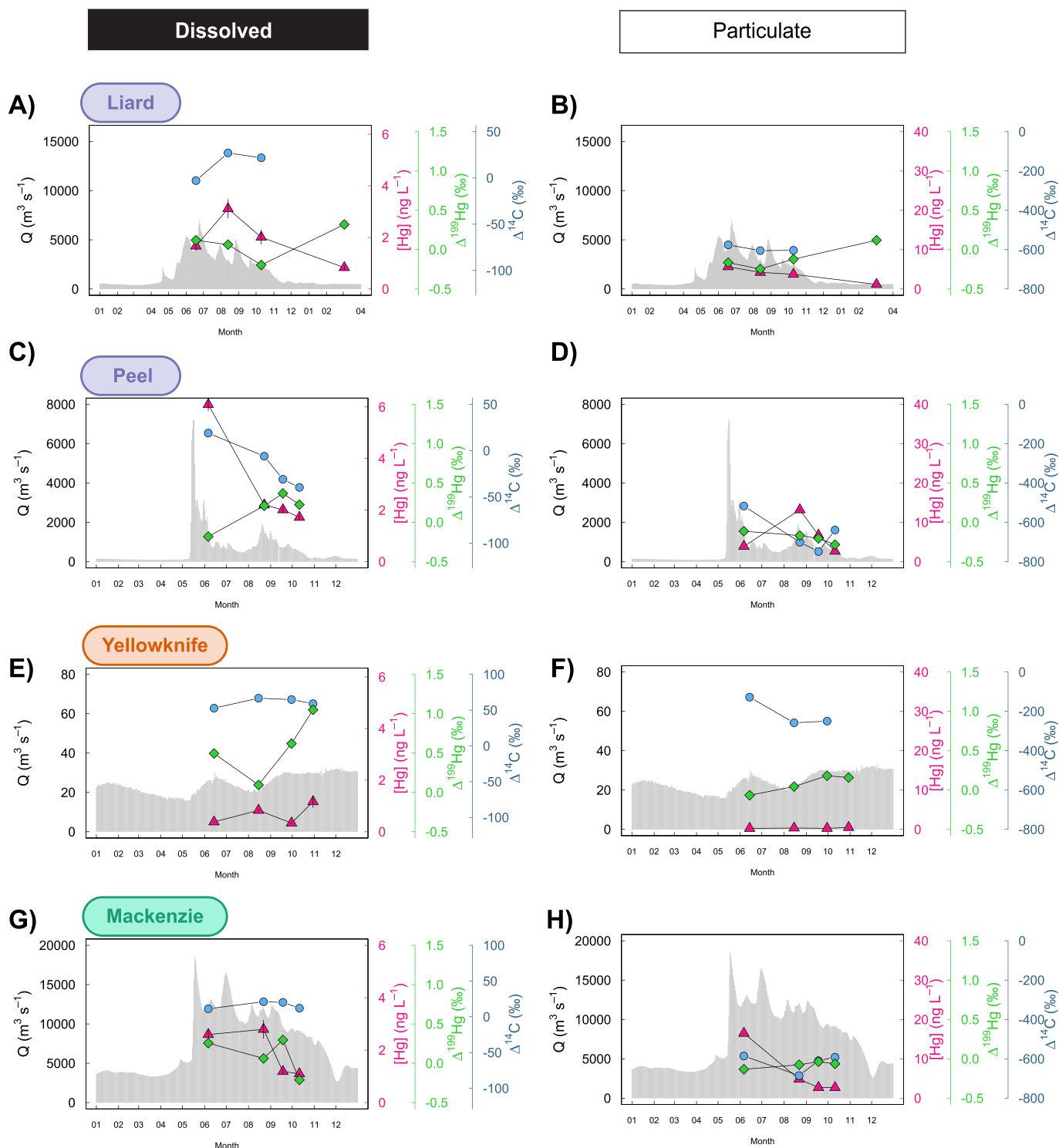


Fig. 6. Hydrograph (gray area, main y axis) of the A, B) Liard River, C, D) Peel River, E, F) Yellowknife River, G, H) Mackenzie River, between January to December 2019 for all sites except the Liard River which extends to April 2020. Superimposed on the hydrograph are the measurements of riverine [Hg] in ng L^{-1} (pink triangles) $\Delta^{199}\text{Hg}$ (‰) (green diamonds) and $\Delta^{14}\text{C}$ -OC (orange circles with sizes representing the [OC] in mg L^{-1}) for the dissolved (A, D, E, G) and particulate (B, D, F, H) fraction. Standard deviation on the [Hg] are superimposed as vertical bars over each symbol, but those of [PHg] are often too small to appear clearly on the figure. Daily discharge measurements from the four rivers included in the seasonal survey were obtained from Environment Canada, under the following station ID: Liard #10ED002, Peel # 10MC002, Yellowknife # 07SB003 and Mackenzie #10LC014. Note that the Yellowknife River is flow-regulated.

destabilization of permafrost soils has triggered a sustained release of ancient DOC to the Mackenzie River (Schwab et al., 2020), a load which may have been accompanied with increased amounts of Hg, according to the correlation identified here (Fig. 3A). The link between riverine [Hg] and $\Delta^{14}\text{C}$ of OC identified provides further indication of the importance of permafrost thaw in mobilizing previously stored OC and Hg in waterways (Bishop et al., 2020; Coquery et al., 1995; St Pierre et al., 2018).

The Slave and Peace rivers, which do not flow over permafrost areas, also transported some of the highest [Hg] and most ^{14}C -depleted OC, part of which may have been mobilized by upstream oil extraction activities. Oil extraction operation carried out in the Peace-Athabasca and Slave River basin may have contributed to the high levels of Hg in these tributaries (Hebert, 2019; Kelly et al., 2010). In recent years, the southern part of the MRB has been heavily affected by forest fires, which can also foster the dissemination of Hg to surrounding environments, (Kumar et al., 2018) as well as the export of older DOC (Turetsky et al., 2015).

Rivers draining the Lowland region transported significantly less Hg (Fig. 1B) with younger (more ^{14}C -enriched) DOC and POC compared with the rivers draining the Mountain region (Fig. 1D) (Campeau et al., 2020). PCA discriminated between two clusters of rivers in the Lowland region (orange symbols). The first included the rivers exclusively draining the Canadian Shield (i.e. Yellowknife, Cameron, Snare) while the second included those found in the Interior Platform (i.e. Hay, Willowlake, Trout) (Fig. 4). Rivers of the latter group contained some of the highest [DOC] and abs_{254} that reflected well the high soil organic carbon content of this region (Tarnocai et al., 2009) with its dense peatland coverage (Tarnocai and Kettles, 2011) that may represent important sources of Hg-bound to DOC (Fig. 5) (Grigal, 2003; Carrie et al., 2012). In comparison, the other tributaries of the Lowland region (i.e. Yellowknife, Snare, Cameron River), contained the lowest [DHg] and [DOC], with the most ^{14}C -enriched DOC, corresponding with the lowest molecular weight (E2/E3, SStratio) and highest freshness (FreshIX) (Figs. 1, 5). These low [Hg] and [OC] are consistent with the region's thin surficial deposits, low soil organic carbon content and abundant small lake and forest coverage.

3.6. Seasonality in Hg and OC sources and potential future release riverine Hg

The coefficient of variation for [PHg], [DOC], $\Delta^{14}\text{C}$ -DOC, $\Delta^{14}\text{C}$ -POC, $\Delta^{199}\text{PHg}$ and $\delta^{202}\text{DHg}$ was larger across rivers (spatial survey) than within a given site (seasonal survey), with the exception of [DHg] where the variability was similar within both the spatial and seasonal survey (Table S4). The opposite occurred for $\Delta^{199}\text{DHg}$ and $\delta^{202}\text{PHg}$ that were both more variable over seasonal scale than spatial scales (Table S4; Fig. 6). However, the variability for $\delta^{202}\text{PHg}$ was generally low in both the spatial and seasonal surveys (Table S4). The seasonal variability in $\Delta^{199}\text{DHg}$ was highest in the Liard River, followed with the Mackenzie, Peel and Yellowknife River. These results suggests that DHg sources may be more variable over time than across rivers of the MRB.

As opposed to the spatial survey, the δ^{202} and Δ^{199} values for the DHg were not significantly more positive than for PHg within individual rivers ($p > 0.05$ for each site, $n = 4$) (Fig. 2). In fact, the median $\Delta^{199}\text{DHg}$ was significantly less positive (closer to zero) in samples collected during the seasonal survey (2019) compared with the spring spatial survey (2018) ($p = 0.009$) (Fig. 2). This suggested that the share of DHg associated with atmospheric deposition varies considerably with changing hydrological conditions. The proportion of DHg associated with terrestrial sources may be comparatively higher in the summer and autumn than during spring flood (Figs. 2, 6). The majority of the annual Hg export from the Mackenzie River to the Arctic Ocean takes place during the spring flood (55% (Zolkos et al., 2020)), highlighting the importance

of considering the distinct sources of DHg and PHg for the annual Hg export in the MRB.

There were no consistent relationships between river discharge and [Hg], [DOC] or IR of Hg or $\Delta^{14}\text{C}$ (Fig. 6). However, differences in [Hg], [OC] and $\Delta^{14}\text{C}$ between groups of rivers identified in the spatial survey were still present in the seasonal sampling (Dunn's test; Lowland (a), Mountain (b), Mackenzie (ab), $p = 0.008$). The correlation between riverine [Hg] and the $\Delta^{14}\text{C}$ of OC was less consistent for the seasonal than for the spatial survey, but the assessment of potential correlations within individual rivers was likely limited by the low number of samples collected over time ($n = 4$ per sites). The importance of the spatial variability over the seasonal variability in [Hg], [OC] and $\Delta^{14}\text{C}$ could suggest that changes in runoff patterns across the MRB will act as an important driver of future trends in river chemistry. While precipitation is on average highest along the Cordilleran mountain ridge, increase in precipitation over the past half-century have been most dramatic in the northeastern banks of the Mackenzie River (+39% in the Great Bear basin) (Bush and Flato, 2018). This could potentially contribute to increase the proportion of Hg originating from the Lowland region in the Mackenzie River in the future. Yet, as permafrost disturbance continues to intensify across the MRB, mobilization of previously stored Hg and ancient OC may continue to increase and contribute to further export to the Arctic Ocean.

4. Conclusion

This study combines various techniques to derive information on the sources of riverine Hg across the MRB. These techniques included isotopic analysis of riverine Hg and OC, together with optical properties of DOM. These data reveal that the dissolved and particulate phases of riverine Hg can be dominated by different sources. While riverine PHg is steadily associated with terrestrial sources, the DHg fraction is supplied, at least partly, from atmospheric sources. Future studies identifying riverine Hg sources must consider separate analysis of dissolved and particulate phases. Bulk analysis of water samples would obscure the individual contributions of different Hg sources and may lead to misinterpretations. Despite these distinct sources, both DHg and PHg were positively associated with the transport of older riverine OC. These correlations translated into a positive correlation between DHg and DOM with higher molecular weight, aromaticity and humic content, which might reflect the Hg-binding potential of DOM. This study demonstrates that the sources of riverine Hg diverge considerably across the landscape of the MRB, in ways that are also consistent with spatial patterns in riverine OC age and quality. Accounting for the diversity of riverine Hg sources will complexify attempts to constrain future release in this rapidly changing river catchment.

Data availability statement

Data are archived on the Bolin Center database (<https://bolin.su.se/data/campeau-2020-2>).

Funding sources

FORMAS (the Swedish government research council for sustainable development), grant # 2017-00660 and #2019-01592.

CRediT authorship contribution statement

Audrey Campeau: Formal analysis, Visualization, Data Curation, Conceptualization, Investigation, Writing – original draft, Writing – review & editing, Validation, Funding acquisition. **Karin Eklöf:** Formal analysis, Conceptualization, Data Curation, Investigation, Methodology, Writing – original draft, Writing – review & editing, Validation. **Anne L. Soerensen:** Formal analysis, Data curation, Conceptualization, Investigation, Methodology, Writing – review & editing, Validation. **Staffan**

Åkerblom: Data Curation, Formal analysis, Conceptualization, Investigation, Methodology, Writing - review & editing, Validation **Shengliu Yuan:** Formal analysis, Data Curation, Conceptualization, Investigation, Methodology, Writing - review & editing, Validation. **Holger Hintelmann:** Formal analysis, Resources, Conceptualization, Investigation, Writing - original draft, Methodology, Writing - review & editing, Validation. **Magdalena Bieroza:** Formal analysis, Data Curation, Conceptualization, Investigation, Methodology, Writing - review & editing, Validation. **Stephan Köhler:** Formal analysis, Data Curation, Conceptualization, Investigation, Methodology, Writing - review & editing, Validation. **Christian Zdanowicz:** Field Work, Resources, Data curation, Formal analysis, Conceptualization, Investigation, Methodology, Writing - original draft Writing - review & editing, Validation, Supervision, Project Administration, Funding acquisition.

Declaration of competing interest

The authors declare that they have no known competing financial interests or personal relationships that could have influence the work reported in this paper.

Acknowledgment

This project was funded by FORMAS, the Swedish government research council for sustainable development (grant # 2017-00660), with additional support from (grant #2019-01529). River sampling in the NWT was conducted under a Scientific Research License issued by the Aurora Research Institute, and with the guidance and/or assistance of community residents and organizations of the following First Nation (FN) groups, to whom we are greatly indebted: South Slave Region: Fort Resolution Metis Council and Deninu K'ue FN (Fort Resolution), and Smith's Landing FN (Fort Smith); North Slave Region: North Slave Métis Alliance (Yellowknife) and Tłı̨chǫ Government (Behchokò); Deh Cho region: Deh Gah Gotie FN (Fort Providence), Łı́ı́łı̨ Kų́ FN (Fort Simpson), and Smbaa K'e FN (Smbaa K'e River); Mackenzie Delta region: Gwich'in Tribal Council (Inuvik) and Tetlit Gwich'Renewal Resources Council (Fort McPherson). In Inuvik, we also benefited from the support of the Western Arctic Research Center and its staff. Sampling on the Peace River in Wood Buffalo National Park, Alberta, was carried out under Park Canada research permit WB-2018-27981 and with kind permission from the Mikisew Cree First Nation. The Salt River FN also provided both guidance and access to the Peace River at Fort Fitzgerald. Hendrick Falk and Steve Kokelj (NWT Geological Survey) and Bruce Stuart (Taiga Environmental Laboratory) gave valuable advice or support in planning the field and lab work. Torbjörn Johannes Erikson and Emmanuël Queyila provided valuable assistance in the field. Claudia Cascone gave valuable guidance during analyses of optical properties (Swedish University of Agricultural Sciences). Analytical services in Ottawa were provided by Paul Middlestead, Wendi Abdi, and Patricia Wickham at the Jan Veizer Stable Isotope Laboratory, and by Carolyn Dziawa, Christabel Jean, Sarah Murseli, and Dr. Xiao-Lei Zhao at the A.E. Lalonde AMS Laboratory.

Appendix A. Supplementary data

Supplementary data to this article can be found online at <https://doi.org/10.1016/j.scitotenv.2021.150808>.

References

AMAP, 2001. In: AMAP (Ed.), AMAP Assessment 2011: Mercury in the Arctic. AMAP, Oslo.

Bergquist, B.A., Blum, J.D., 2007. Mass-dependent and -independent fractionation of Hg isotopes by photoreduction in aquatic systems. *Science* 318, 417–420.

Bieroza, M.Z., Heathwaite, A.L., 2016. Unravelling organic matter and nutrient biogeochemistry in groundwater-fed rivers under baseflow conditions: uncertainty in in situ high-frequency analysis. *Sci. Total Environ.* 572, 1520–1533.

Bishop, K., Shanley, J.B., Riscassi, A., de Wit, H.A., Eklöf, K., Meng, B., et al., 2020. Recent advances in understanding and measurement of mercury in the environment: terrestrial Hg cycling. *Sci. Total Environ.* 721, 137647.

Blum, J.D., Bergquist, B.A., 2007. Reporting of variations in the natural isotopic composition of mercury. *Anal. Bioanal. Chem.* 388, 353–359.

Braune, B., Chetelat, J., Amyot, M., Brown, T., Clayden, M., Evans, M., et al., 2015. Mercury in the marine environment of the Canadian Arctic: review of recent findings. *Sci. Total Environ.* 509–510, 67–90.

Bravo, A.G., Kothawala, D.N., Attermeyer, K., Tessier, E., Bodmer, P., Ledesma, J.L.J., et al., 2018. The interplay between total mercury, methylmercury and dissolved organic matter in fluvial systems: a latitudinal study across Europe. *Water Res.* 144, 172–182.

Brigham, M.E., Wentz, D.A., Aiken, G.R., Krabbenhoft, D.P., 2009. Mercury cycling in stream ecosystems. 1. Water column chemistry and transport. *Environ. Sci. Technol.* 43, 2720–2725.

Brown, J., Ferrians Jr., O.J., Heginbottom Jr., J.A., Melnikov Jr., E.S., 2002. Circum-Arctic map of permafrost and ground-ice conditions. Circum-Pacific Map. NSIDC, National Snow and Ice Data Center, Boulder, Colorado USA 2 V.

Bush, E., Flato, G.M., 2018. About this report: Chapter 1 in Canada's changing climate report. In: EBaDS, Lemmen (Ed.) Government of Canada, Ottawa, Ontario, pp. 7–23.

Cameron, A.R., Beaton, A.P., 2000. Coal resources of Northern Canada with emphasis on Whitehorse Trough, Bonnet Plume Basin and Brackett Basin. Geological Survey of Canada Contribution No. 1999-127.1. *Int. J. Coal Geol.* 43, 187–210.

Campeau, A., Soerensen, A.L., Martma, T., Åkerblom, S., Zdanowicz, C., 2020. Controls on the 14C content of dissolved and particulate organic carbon mobilized across the Mackenzie River Basin, Canada. 34.

Carrie, J., Sanei, H., Goodarzi, F., Stern, G., Wang, F., 2009. Characterization of organic matter in surface sediments of the Mackenzie River Basin, Canada. 77, 416–423.

Carrie, J., Stern, G.A., Sanei, H., Macdonald, R.W., Wang, F.Y., 2012. Determination of mercury biogeochemical fluxes in the remote Mackenzie River basin, Northwest Canada, using speciation of sulfur and organic carbon. *Appl. Geochem.* 27, 815–824.

Castello, L., Zhulidov, A.V., Gurtovaya, T.Y., Robarts, R.D., Holmes, R.M., Zhulidov, D.A., et al., 2014. Low and declining mercury in arctic russian rivers. *Environ. Sci. Technol.* 48, 747–752.

Chen, J., Hintelmann, H., Feng, X., Dimock, B., 2012. Unusual fractionation of both odd and even mercury isotopes in precipitation from Peterborough, ON, Canada. 90, 33–46.

Chen, J., Hintelmann, H., Zheng, W., Feng, X., Cai, H., Wang, Z., et al., 2016. Isotopic evidence for distinct sources of mercury in lake waters and sediments. *Chem. Geol.* 426, 33–44.

Coquery, M., Cossa, D., Martin, J.M., 1995. The distribution of dissolved and particulate mercury in three Siberian estuaries and adjacent Arctic coastal waters. *Water Air Soil Pollut.* 80, 653–664.

Crann, C.A., Murseli, S., St-Jean, G., Zhao, X., Clark, I.D., Kieser, W.E., 2017. First status report on radiocarbon sample preparation techniques at the A.E. Lalonde AMS Laboratory (Ottawa, Canada). *Radiocarbon* 59, 695–704.

Dastoor et al., n.d. Dastoor A, Angot, H., Bieser, J., Christensen, J.H., Douglas, T.A., Heimbürger-Boavida, L.-E., Jiskra, M., Mason, R.P., McLagan, D.S., Obrist, D., Outridge, P.M., Petrova, M.V., Ryjkov, A., St. Pierre, K.A., Schartup, A.T., Soerensen, A.L., Travnikov, O., Toyota, K., Wilson, S.J. and Zdanowicz, C. Arctic mercury cycling. *Nature Reviews Earth & Environment* Submitted; (ms # NATREVEARTHENVIRON-21-077V1B).

Davis, B.E., 2005. A Guide to the Proper Selection and Use of Federally Approved Sediment and Water-Quality Samplers. Open File Report 2005-1087, Vicksburg, MS 20 p.

De Haan, H., De Boer, T., 1987. Applicability of light absorbance and fluorescence as measures of concentration and molecular size of dissolved organic carbon in humic Lake Tjeukemeer. *Water Res.* 21, 731–734.

Demers, J.D., Blum, J.D., Zak, D.R., 2013. Mercury isotopes in a forested ecosystem: implications for air-surface exchange dynamics and the global mercury cycle. *Glob. Biogeochem. Cycl.* 27, 222–238.

Dietz, R., Sonne, C., Basu, N., Braune, B., O'Hara, T., Letcher, R.J., et al., 2013. What are the toxicological effects of mercury in Arctic biota? *Sci. Total Environ.* 443, 775–790.

Dittman, J.A., Shanley, J.B., Driscoll, C.T., Aiken, G.R., Chalmers, A.T., Towse, J.E., 2009. Ultraviolet absorbance as a proxy for total dissolved mercury in streams. *Environ. Pollut.* 157, 1953–1956.

Driscoll, C.T., Mason, R.P., Chan, H.M., Jacob, D.J., Pirrone, N., 2013. Mercury as a global pollutant: sources, pathways, and effects. *Environ. Sci. Technol.* 47, 4967–4983.

Eklöf, K., Folster, J., Sonesten, L., Bishop, K., 2012. Spatial and temporal variation of THg concentrations in run-off water from 19 boreal catchments, 2000–2010. *Environ. Pollut.* 164, 102–109.

Emmerton, C.A., Graydon, J.A., Gareis, J.A., St Louis, V.L., Lesack, L.F., Banack, J.K., et al., 2013. Mercury export to the Arctic Ocean from the Mackenzie River, Canada. 47, 7644–7654.

Fulton, R.J., 2014. Surficial geology of Canada; Map195. Geological Survey of Canada. Canadian Geoscience.

Gaur, A., Gaur, A., Yamazaki, D., Simonovic, S.P., 2019. Flooding related consequences of climate change on Canadian cities and flow regulation infrastructure. *Water* 11.

Graydon, J.A., Emmerton, C.A., Lesack, L.F., Kelly, E.N., 2009. Mercury in the Mackenzie River delta and estuary: concentrations and fluxes during open-water conditions. *Sci. Total Environ.* 407, 2980–2988.

Griffin, C.G., McClelland, J.W., Frey, K.E., Fiske, G., Holmes, R.M., 2018. Quantifying CDOM and DOC in major Arctic rivers during ice-free conditions using landsat TM and ETM + data. *Remote Sens. Environ.* 209, 395–409.

Grigal, D.F., 2003. Mercury sequestration in forests and peatlands: a review. *J. Environ. Qual.* 32, 393–405.

Guevara, S.R., Horvat, M., 2013. Stability and behaviour of low level spiked inorganic mercury in natural water samples. *Anal. Methods* 5.

- Haitzer, M., Aiken, G.R., Ryan, J.N., 2002. Binding of mercury(II) to dissolved organic matter: the role of the mercury-to-DOM concentration ratio. *Environ. Sci. Technol.* 36, 3564–3570.
- Hebert, C.E., 2019. The river runs through it: the Athabasca River delivers mercury to aquatic birds breeding far downstream. *PLoS One* 14, e0206192.
- Helms, J.R., Stubbins, A., Ritchie, J.D., Minor, E.C., Kieber, D.J., Mopper, K., 2008. Absorption spectral slopes and slope ratios as indicators of molecular weight, source, and photobleaching of chromophoric dissolved organic matter. *Limnol. Oceanogr.* 53, 955–969.
- Hilton, R.G., Galy, V., Gaillardet, J., Dellinger, M., Bryant, C., O'Regan, M., et al., 2015. Erosion of organic carbon in the Arctic as a geological carbon dioxide sink. *Nature* 524, 84–87.
- Holmes, R.M., JW, McClelland, Tank, S.E., RGM, Spencer, Shiklomanov, A.L., 2018. In: AGR, Observatory (Ed.), *Water Quality Dataset Version 20181010*.
- Huang, Q., Liu, Y.L., Chen, J.B., Feng, X.B., Huang, W.L., Yuan, S.L., et al., 2015. An improved dual-stage protocol to pre-concentrate mercury from airborne particles for precise isotopic measurement. *J. Anal. At. Spectrom.* 30, 957–966.
- Jiskra, M., Wiederhold, J.G., Skyllberg, U., Kronberg, R.M., Hajdas, I., Kretzschmar, R., 2015. Mercury deposition and re-emission pathways in boreal forest soils investigated with Hg isotope signatures. *Environ. Sci. Technol.* 49, 7188–7196.
- Kelly, E.N., Schindler, D.W., Hodson, P.V., Short, J.W., Radmanovich, R., Nielsen, C.C., 2010. Oil sands development contributes elements toxic at low concentrations to the Athabasca River and its tributaries. *Proc. Natl. Acad. Sci. U. S. A.* 107, 16178–16183.
- Kokelj, S.V., Jenkins, R.E., Milburn, D., Burn, C.R., Snow, N., 2005. The influence of thermokarst disturbance on the water quality of small upland lakes, Mackenzie Delta region, Northwest Territories, Canada. 16, 343–353.
- Kuhn, C., de Matos, Valerio A., Ward, N., Loken, L., Sawakuchi, H.O., Kampel, M., et al., 2019. Performance of Landsat-8 and Sentinel-2 surface reflectance products for river remote sensing retrievals of chlorophyll-a and turbidity. *Remote Sens. Environ.* 224, 104–118.
- Kumar, A., Wu, S., Huang, Y., Liao, H., Kaplan, J.O., 2018. Mercury from wildfires: global emission inventories and sensitivity to 2000–2050 global change. *Atmos. Environ.* 173, 6–15.
- Lacelle, D., Brooker, A., Fraser, R.H., Kokelj, S.V., 2015. Distribution and growth of thaw slumps in the Richardson Mountains-Peel Plateau region, northwestern Canada. *Geomorphology* 235, 40–51.
- Lang, S.Q., McIntyre, C.P., Bernasconi, S.M., Früh-Green, G.L., Voss, B.M., Eglinton, T.I., et al., 2016. Rapid 14 C analysis of dissolved organic carbon in non-saline waters. *Radiocarbon* 58, 505–515.
- Latifovic, R., Pouliot, D., Olthoff, I., 2017. Circa 2010 land cover of Canada: local optimization methodology and product development. *Remote Sens.* 9 (11). <https://doi.org/10.3390/rs9111098>.
- Lavoie, R.A., Amyot, M., Lapierre, J.F., 2019. Global meta-analysis on the relationship between mercury and dissolved organic carbon in freshwater environments. 124, 1508–1523.
- Lawaetz, A.J., Stedmon, C.A., 2009. Fluorescence intensity calibration using the Raman scatter peak of water. *Appl. Spectrosc.* 63, 936–940.
- Leitch, D.R., Carrie, J., Lean, D., Macdonald, R.W., Stern, G.A., Wang, F., 2007. The delivery of mercury to the Beaufort Sea of the Arctic Ocean by the Mackenzie River. *Sci. Total Environ.* 373, 178–195.
- Lescord, G.L., Emilson, E.J.S., Johnston, T.A., Branfireun, B.A., Gunn, J.M., 2018. Optical properties of dissolved organic matter and their relation to mercury concentrations in water and biota across a remote freshwater drainage basin. *Environ. Sci. Technol.* 52, 3344–3353.
- Lim, A.G., Jiskra, M., Sonke, J.E., Loiko, S.V., Kosykh, N., Pokrovsky, O.S., 2020. A revised pan-Arctic permafrost soil Hg pool based on Western Siberian peat Hg and carbon observations. *Biogeochemistry* 17, 3083–3097.
- McKnight, D.M., Boyer, E.W., Westerhoff, P.K., Doran, P.T., Kulbe, T., Andersen, D.T., 2001. Spectrofluorometric characterization of dissolved organic matter for indication of precursor organic material and aromaticity. *Limnol. Oceanogr.* 46, 38–48.
- Nasr, M., Ogilvie, J., Castonguay, M., Rencz, A., Arp, P.A., 2011. Total Hg concentrations in stream and lake sediments: discerning geospatial patterns and controls across Canada. *Appl. Geochem.* 26, 1818–1831.
- Obrist, D., Agnan, Y., Jiskra, M., Olson, C.L., Colegrove, D.P., Hueber, J., et al., 2017. Tundra uptake of atmospheric elemental mercury drives Arctic mercury pollution. *Nature* 547, 201–204.
- Ohno, T., 2002. Fluorescence inner-filtering correction for determining the humification index of dissolved organic matter. *Environ. Sci. Technol.* 36, 742–746.
- Pelletier, J.D., Broxton, P.D., Hazenberg, P., Zeng, X., Troch, P.A., Niu, G.Y., et al., 2016. A gridded global data set of soil, intact regolith, and sedimentary deposit thicknesses for regional and global land surface modeling. *J. Adv. Model. Earth Syst.* 8, 41–65.
- Raymond, P.A., McClelland, J.W., Holmes, R.M., Zhulidov, A.V., Mull, K.C., Peterson, B.J., et al., 2007. Flux and age of dissolved organic carbon exported to the Arctic Ocean: a carbon isotopic study of the five largest arctic rivers. *Glob. Biogeochem. Cycl.* 21 n/a-n/a.
- Rice, E.W., Baird, R.B., ADE, Eaton, 2017. Standard methods for the examination of water and wastewater Method 2540 D. Total suspended solids. American Public Health Association (APHA), American Water Works Association (AWWA), Water Environment Federation (WEF), Washington DC, USA.
- Roberts, M.L., Elder, K.L., Jenkins, W.J., Gagnon, A.R., Xu, L., Hlavinka, J.D., et al., 2019. 14C blank corrections for 25–100 µg samples at the National Ocean Sciences AMS Laboratory. *Radiocarbon* 61, 1403–1411.
- Rood, S.B., Kaluthota, S., Philipsen, L.J., Rood, N.J., Zanewich, K.P., 2017. Increasing discharge from the Mackenzie River system to the Arctic Ocean. *Hydrol. Process.* 31, 150–160.
- Schuster, P.F., Striegl, R.G., Aiken, G.R., Krabbenhoft, D.P., Dewild, J.F., Butler, K., et al., 2011. Mercury export from the Yukon River basin and potential response to a changing climate. *Environ. Sci. Technol.* 45, 9262–9267.
- Schuster, P.F., Schaefer, K.M., Aiken, G.R., Antweiler, R.C., Dewild, J.F., Gryzic, J.D., et al., 2018. Permafrost stores a globally significant amount of mercury. *Geophys. Res. Lett.* 45, 1463–1471.
- Schwab, M.S., Hilton, R.G., Raymond, P.A., Haghpor, N., Amos, E., Tank, S.E., et al., 2020. 47.
- Skyllberg, U., Bloom, P.R., Qian, J., Lin, C.M., Bleam, W.F., 2006. Complexation of mercury (II) in soil organic matter: EXAFS evidence for linear two-coordination with reduced sulfur groups. *Environ. Sci. Technol.* 40, 4174–4180.
- Soerensen, A.L., Jacob, D.J., Schartup, A.T., Fisher, J.A., Lehnher, I., St. Louis, V.L., 2016. A mass budget for mercury and methylmercury in the Arctic Ocean. *Glob. Biogeochem. Cycl.* 30, 560–575.
- Sonke, J.E., Teisserenc, R., Heimburger-Boavida, L.E., Petrova, M.V., Maruscak, N., Le Dantec, T., et al., 2018. Eurasian river spring flood observations support net Arctic Ocean mercury export to the atmosphere and Atlantic Ocean. *Proc. Natl. Acad. Sci. U. S. A.* 115, E11586–E11594.
- St Pierre, K.A., Zolkos, S., Shakil, S., Tank, S.E., St. Louis, V.L., Kokelj, S.V., 2018. Unprecedented increases in total and methyl mercury concentrations downstream of retrogressive thaw slumps in the Western Canadian Arctic. *Environ. Sci. Technol.* 52, 14099–14109.
- Stein, R., Macdonald, R.W., 2004. *The Organic Carbon Cycle in the Arctic Ocean*. Springer-Verlag, Berlin Heidelberg.
- Stern, G.A., Macdonald, R.W., Outridge, P.M., Wilson, S., Chetelat, J., Cole, A., et al., 2012. How does climate change influence Arctic mercury? *Sci. Total Environ.* 414, 22–42.
- St-Jean, G., Kieser, W.E., Crann, C.A., Murseli, S., 2017. Semi-automated equipment for CO₂ purification and graphitization at the AE Lalonde AMS Laboratory (Ottawa, Canada). *Radiocarbon* 59, 941–956.
- Stuiver, M., Polach, H.A., 1977. Discussion; reporting of C-14 data. *Radiocarbon* 19, 355–363.
- Tank, S.E., Striegl, R.G., McClelland, J.W., Kokelj, S.V., 2016. Multi-decadal increases in dissolved organic carbon and alkalinity flux from the Mackenzie drainage basin to the Arctic Ocean. *Environ. Res. Lett.* 11.
- Tarnocai, C., Kettles, Lacette, 2011. *Peatlands of Canada*.
- Tarnocai, C., Canadell, J.G., Schuur, E.A.G., Kuhry, P., Mazhitova, G., Zimov, S., 2009. Soil organic carbon pools in the northern circumpolar permafrost region. *Glob. Biogeochem. Cycl.* 23 n/a-n/a.
- Team RC, 2020. R: A language and environment for statistical computing. R Foundation for Statistical Computing, Vienna, Austria. <https://www.R-project.org/>.
- Treat, C.C., Jones, M.C., 2018. Near-surface permafrost aggradation in northern hemisphere peatlands shows regional and global trends during the past 6000 years. *The Holocene* 28, 998–1010.
- Turetsky, M.R., Benscoter, B., Page, S., Rein, G., Van Der Werf, G.R., Watts, A., 2015. Global vulnerability of peatlands to fire and carbon loss. *Nat. Geosci.* 8, 11–14.
- Vermilyea, A.W., Nagorski, S.A., Lamborg, C.H., Hood, E.W., Scott, D., Swarr, G.J., 2017. Continuous proxy measurements reveal large mercury fluxes from glacial and forested watersheds in Alaska. *Sci. Total Environ.* 599–600, 145–155.
- Wang, F., Outridge, P.M., Feng, X., Meng, B., Heimburger-Boavida, L.E., Mason, R.P., 2019. How closely do mercury trends in fish and other aquatic wildlife track those in the atmosphere? - Implications for evaluating the effectiveness of the Minamata Convention. *Sci. Total Environ.* 674, 58–70.
- Wickham, H., Averick, M., Bryan, J., Chang, W., McGowan, L., François, R., et al., 2019. Welcome to the tidyverse. *J. Open Source Softw.* 4.
- Wiederhold, J.G., Cramer, C.J., Daniel, K., Infante, I., Bourdon, B., Kretzschmar, R., 2010. Equilibrium mercury isotope fractionation between dissolved Hg(II) species and thiol-bound Hg. *Environ. Sci. Technol.* 44, 4191–4197.
- Xu, J., Morris, P.J., Liu, J., Holden, J., 2018. PEATMAP: refining estimates of global peatland distribution based on a meta-analysis. *Catena* 160, 134–140.
- Zheng, W., Hintelmann, H., 2010. Nuclear field shift effect in isotope fractionation of mercury during abiotic reduction in the absence of light. *J. Phys. Chem. A* 114, 4238–4245.
- Zheng, J., RoyChowdhury, T., Yang, Z., Gu, B., Wullschlegel, S.D., Graham, D.E., 2018. Impacts of temperature and soil characteristics on methane production and oxidation in Arctic tundra. *Biogeochemistry* 15, 6621–6635.
- Zhou, Y., Guo, H., Lu, H., Mao, R., Zheng, H., Wang, J., 2015. Analytical methods and application of stable isotopes in dissolved organic carbon and inorganic carbon in groundwater. *Rapid Commun. Mass Spectrom.* 29, 1827–1835.
- Zhou, J., Obrist, D., Dastoor, A., Jiskra, M., Ryjkov, A., 2021. Vegetation uptake of mercury and impacts on global cycling. *Nat. Rev. Earth Environ.* 2, 269–284.
- Zolkos, S., Tank, S.E., Kokelj, S.V., 2018. Mineral weathering and the permafrost carbon-climate feedback. *Geophys. Res. Lett.* 45, 9623–9632.
- Zolkos, S., Krabbenhoft, D.P., Suslova, A., Tank, S.E., McClelland, J.W., Spencer, R.G.M., et al., 2020. Mercury export from Arctic Great Rivers. *Environ. Sci. Technol.* 54, 4140–4148.